A Differentiable Method for Low-Fidelity Analysis of Permanent-Magnet Synchronous Motors

Zeyu Cheng* and Shuofeng Zhao†
San Diego State University, San Diego, California, 92182

Luca Scotzniovsky‡
University of California San Diego, La Jolla, California, 92023

Gabriel Rodriguez§ and Chris Mi¶
San Diego State University, San Diego, California, 92182

John T. Hwang‖
University of California San Diego, La Jolla, California, 92023

To facilitate the design and optimization of permanent magnet synchronous motors (PMSMs), a fast and accurate analytical method for modeling is necessary. This paper presents a low-fidelity, differentiable model for the performance of PMSMs. The approach is based on the magnetic equivalent circuit (MEC), empirical motor geometry model, and motor integrated control strategies to obtain fast and accurate results. Compared with the existing Finite Element Method (FEM), the proposed method has flexible motor geometry parametric analysis, low computational burden, and accurate results with errors in losses and efficiency less than 3%. The validation shows that the proposed method can successfully predict the magnetic performance of PMSMs, such as Electromotive Force (EMF), torque, magnetic flux density, and losses.

I. Nomenclature

A	=	electric loading, which represents the linear current density inside the stator inner diameter
B_{air}	=	magnetic loading, which represents the average flux density over the air-gap
B_t	=	magnetic flux density along the tooth
B_{ys}	=	magnet flux density along the yoke
B_{r20}	=	residual magnetic flux density at T = 20°
C	=	constant coefficient
D_i	=	internal diameter of the stator
I_d	=	current at d axis
I_q	=	current at q axis
I_{lim}	=	maximum current operating in the PMSM
K_{fe}	=	lamination coefficient
K_{IL}	=	rate of irreversible loss
k	=	coefficient of smooth integration
k_e	=	Steinmetz eddy-loss coefficient
k_h	=	Steinmetz hysteresis coefficient
L_{ef}	=	effective stack length of the motor
L_d	=	inductance at d axis
L_q	=	inductance at q axis

*Ph.D. Student, Department of Electrical and Computer Engineering
†Postdoctoral Scholar, Department of Electrical and Computer Engineering
‡Ph.D. Student, Department of Mechanical and Aerospace Engineering, AIAA student member
§Graduate Student, Department of Mechanical Engineering
¶Distinguished Professor, Department of Electrical and Computer Engineering
‖Assistant Professor, Department of Mechanical and Aerospace Engineering, AIAA senior member

n	=	rotor speed
n_N	=	rated speed
n_h	=	alpha exponent for hysteresis loss
P_o	=	output power
p	=	number of pair of poles
p_1	=	derivative operator
R_s	=	phase resistance
t	=	estimated operation temperature
T_{em}	=	electromagnetic torque
T_{em}^*	=	per-unit value of reference torque
U_d	=	voltage at d axis
U_q	=	voltage at q axis
U_{lim}	=	maximum voltage in the DC-Bus
V	=	volume of motor
W_m	=	base mechanical loss
Z	=	total number of slots
α_p	=	pole spanning coefficient
$\cos\varphi$	=	power factor
η	=	efficiency
θ_{ssi}	=	angular of slot opening
λ_δ	=	total conductance of stator, air gap, and rotor
λ_f	=	conductance of magnetic bridge
λ_s	=	total leakage conductance through nonmagnetic material
λ_σ	=	conductance of magnet
ψ_m	=	magnet flux linkage
ϕ_r	=	residual flux of each pole
ϕ_m	=	main flux through the motor
ϕ_f	=	flux leakage in magnetic bridges
ϕ_s	=	flux leakage in rotor and stator
ϕ_δ	=	flux leakage in other non-magnetic material
ω	=	angular velocity
ρ	=	steel density

II. Introduction

The financial and environmental concerns regarding greenhouse gas emissions have motivated the aviation industry to move towards electrification [1]. As part of this movement, the concept of electric vertical take-off and landing (eVTOL) aircraft has the potential to have a transformative impact on urban transportation. The technological advancement in batteries, motors, and electric vehicles (EVs) has shown the possibilities of eVTOL capability if sufficiently high power components and battery technologies are developed [2].

Motors are crucial components in eVTOL aircraft. Key figures of merits for the motors such as power density, efficiency, and mass, directly affect the performance of the aircraft. In the field of electric motor, Permanent Magnet Synchronous Motors (PMSM) have been widely implemented in electric aircraft due to the advantage of high power density over its counterparts such as induction motors and switch reluctance motors [3]. The performance of PMSM is heavily dependent on properly designed geometry and high-energy density magnets, such as NdFeB, to produce a strong magnetic field. PMSMs can use these rare-earth magnet materials to bring such benefits as no excitation loss, lower copper loss, high magnetic flux density along the airgap, and high-power factor. As a result, advanced approaches for PMSM design and analysis in aircraft applications have been given much attention in recent years.

The optimal design of PMSM involves hundreds of variables such as geometric values, nonlinear materials characteristics, and input variables from other disciplines. Further, the generalization of motors is difficult to achieve due to the diversity of rotor topology. To satisfy the requirements for analysis accuracy and acceptable time consumption, several simplification techniques have been developed as an advancement in the rapid and accurate finite element methods (FEM) for PMSM optimization. Ionel proposed a method that analyzed average torque of PMSM during each single magnetostatic simulation [4]. Recently, Ionel and Gennadi introduced a computationally efficient FE method of calculating the radial and tangential flux density waveforms [5], which can reduce computational losses and save time.

However, due to the complexity of FE-based models, these high-fidelity models have a high computational cost, especially when a very dense mesh is required to maintain accuracy. Low-fidelity models can be employed in the optimal design framework as a complement of high-fidelity models to produce sufficiently accurate preliminary results for further evaluation with very low computational cost [6]. Hemeida [7] and Cao [8] proposed a combined solution of Maxwell's equations and magnetic equivalent circuit method to obtain accurate results in the calculation of PMSM parameters. This is especially meaningful when put into the context of eVTOL motor design where there are a large number of variables because of the diversity in possible eVTOL architectures. A large-scale multidisciplinary design optimization method based on gradient-based optimization was presented in [9][10].

In this paper, we propose a low-fidelity PMSM sizing model for the optimization of eVTOL aircraft that can evaluate the performance of PMSM based solely on its output power and base speed. The proposed approach combines the essences of pragmatic sizing, magnetic equivalent circuit, and important motor control metrics. It delivers sufficiently accurate efficiency maps in a computational-efficient manner to facilitate further design. The proposed approach is validated by comparing the calculated motor performance indices to those from the high fidelity FE method. Section III describes the motor topology and specification used in this paper and the details of each modeling methodology for motor geometry parametric, MEC, and discrete control strategies. Section IV shows the validation of the low-fidelity model and comparison with the FEM model, which was based on Ansoft Maxwell and MotorCAD software.

III. Modeling Methodology

A. Problem Description

The outputs of the low-fidelity model include geometry size, efficiency, and other crucial parameters calculated via magnetic equivalent circuit analysis. [11]. The low-fidelity model has been implemented and tested using a radial interior PMSM with 36-slot, 12-poles. The stator has a double-layer integrated winding distribution, powered by three-phase sinusoidal current. The three phase coils are star-connected. The magnet, embedded in the rotor and radially magnetized, has a linear demagnetization curve, coupling with the temperature coefficient. The motor geometry is chosen from the sizing model. The baseline motor model is analyzed using a 2D simulation.

As depicted in Fig. 1, the low-fidelity model is divided into two main sub-models: sizing model and performance model. The geometry parameters can be calculated from the sizing model. The performance model adopts magnetic equivalent circuit (MEC) calculation and smooth formulation of Maximum Torque Per Ampere (MTPA) and flux-weakening control strategies to evaluate the performance of PMSM using the motor geometry from the sizing model. The low-fidelity model is represented in an implicit manner to relate the unknown electromagnetic torque and efficiency to the known load and speed.

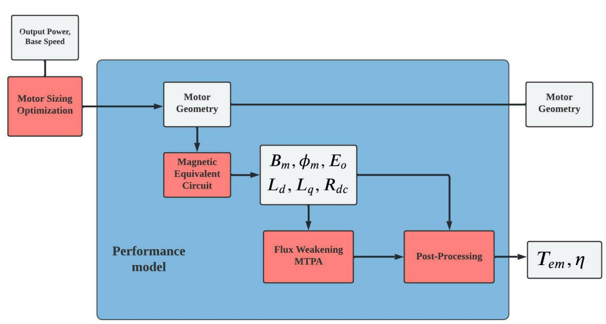

Fig. 1 Low-fidelity model architecture.

B. Motor Geometry Analysis

The motor sizing is proportional to torque and is derived based on simplified empirical relationships found in [12], shown in Eq. 1. Equation 1 represents the geometry size of the PMSM as a function of the basic magnetic variables and output power. The internal diameter and effective length of the motor, main dimensions of the motor frame, can be evaluated from Eq. 1.

$$V = D_i^2 L_{ef} = \frac{6.1 P_o}{CAB_{air} n\eta \cos\varphi} \tag{1}$$

Given any output power and speed, the large-scale geometric parameters such as stator diamter and motor length can be calculated from Eq. 1. However, these main dimensions are insufficient for evaluating motor performance. Fine motor sizing parameters such as slot size and magnet topology also have a significant impact on the PMSM. Therefore, integrating the internal motor size analysis into the motor sizing model is necessary for a comprehensive analysis of electric motor performance. The main parameters of the stator slot are shown in Fig. 2. Detailed steps of internal motor size analysis are shown in Table 1.

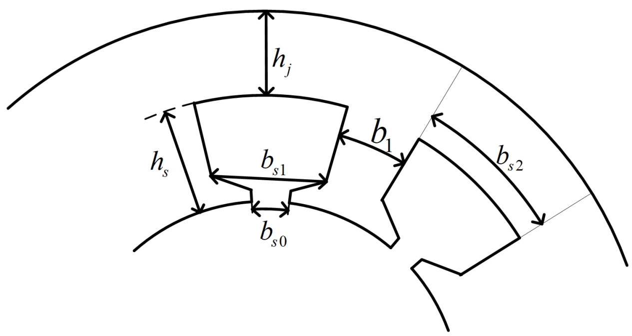

Fig. 2 Main Dimension of Stator Slot.

Table 1 Design variables of slot.

Items	Nomenclature	Equation
Tooth pitch	t_1	$t_1 = \frac{\pi D_i}{Z}$
Tooth width	b_1	$b_1 = \frac{t_1 B_{air}}{K_{fe} B_t}$
Yoke height	h_j	$h_j = \frac{\tau \alpha_p B_{air}}{2K_{fe} B_{ys}}$
slot depth	h_s	$h_s = \frac{D_1 - D_i}{2} - h_j$
slot opening	b_{s0}	$b_{s0} = \frac{\theta_{ssi} \pi D_i}{360}$
Slot Width (bottom)	b_{s1}	$b_{s1} = \frac{\pi(D_i + 2h_{os} + 2h_k)}{Z} - b_1$
Slot Width (Top)	b_{s2}	$b_{s2} = \frac{\pi(D_i + 2h_{slot})}{Z} - b_1$

C. Magnetic Equivalent Circuit

1. Equivalent Circuit

Magnetic variables, such as air-gap flux, magnetic flux density, and back EMF, are crucial for evaluating the performance of the motor. To ensure the accuracy of high-fidelity model, these parameters are usually calculated using the FE method, which is highly dependent on the mesh density surrounding the geometry [13]. The classical FE-based model, on the other hand, restricts the design space due to long computation times. The low-fidelity model adopts magnetic equivalent circuit analysis to simplify the complexity of FE-method, achieving rapid simulation and minimum iteration effort. The magnetic equivalent circuit of this PMSM is shown in Fig. 3(a) [11]. Solving the MEC, electromagnetic quantities can be derived. Fig. 3(b) shows the flux distribution of the PMSM under no-load condition. The impact of leakage flux, which occurs in magnetic bridge I and II, is accounted for in the MEC approach.

2. Magnet Operation Point

The characteristics of the rare-earth permanent magnet material is a crucial factor in determining the design of electric motors. Temperature influences and non-linear permeability curve is taken into account in MEC method. The

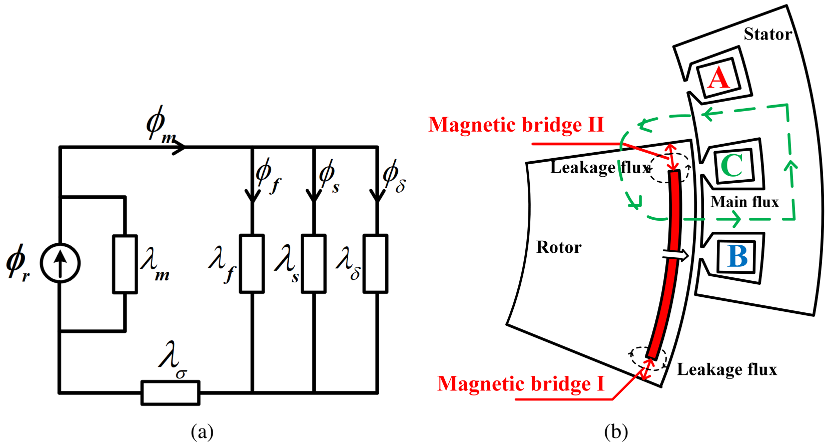

Fig. 3 Magnetic equivalent circuit of the baseline PMSM (a) Equivalent circuit for the PMSM and (b) Illustration for no-load flux distribution of the PMSM.

residual magnetic flux density B_r of the magnets are expressed in Eq. 2.

$$B_r = [1 + (t - 20)\frac{\alpha_{B_r}}{100}](1 - \frac{K_{IL}}{100})B_{r20} \tag{2}$$

As can be seen from Fig.3(a), the residual magnetic flux ϕ_r is only theoretically flux source. The flux losses from magnet conductance and other parts of the motor are inevitable. The effective flux provided by magnets is always less than the residual flux. In addition, temperature can alter the operation point of the magnet, as mentioned above. In the MEC approach, it is essential to determine the practical magnet operating point. Figure 4(a) shows the detailed steps of graphic analysis to find the magnet operation point and analyze saturation effect in the york, teeth, and magnetic bridge. Figure 4(b) shows the results from finding the operation point of the magnet under no-load condition. Dichotomy method is adopted in solving the operation point of magnet. Through Fig.4(a), the magnetic flux density along the air gap B_{air} can also be solved. Once B_{air} and motor geometry are determined, the Back-EMF, inductance at d and q axis, torque and output power can be calculated through the MEC method.

D. Flux Weakening

Consideration of flux weakening and MTPA in a low-fidelity model aims to generate a realistic operation curve for the PMSM and evaluate its performance under a variety of conditions. In the analysis below, all variables and PMSM mathematical model are expressed in normalized terms and established in the d-q rotor coordinate system. The voltage equations in the d-q axis are expressed in Eq. 3:

$$\begin{bmatrix} U_d \\ U_q \end{bmatrix} = \begin{bmatrix} R_s + p_1 L_d & -\omega L_q \\ \omega L_d & R_s + p_1 L_q \end{bmatrix} \begin{bmatrix} i_d \\ i_q \end{bmatrix} + \omega \begin{bmatrix} 0 \\ \psi_m \end{bmatrix} \tag{3}$$

The low-fidelity model does not consider dynamic processes. Therefore, time variable, p_1, can be ignored. The voltage equations are then demonstrated in Eq. 4:

$$\begin{bmatrix} U_d \\ U_q \end{bmatrix} = \begin{bmatrix} R_s & -\omega L_q \\ \omega L_d & R_s \end{bmatrix} \begin{bmatrix} i_d \\ i_q \end{bmatrix} + \omega \begin{bmatrix} 0 \\ \psi_m \end{bmatrix} \tag{4}$$

Due to physical constraints, the PMSM model is subjected to the following limits. The stator current is limited to the maximum continuous armature current or to the maximum current that the inverter can provide. Also, the maximum voltage is limited to the maximum available voltage on the DC-Bus. Considering the rated values provided by the eVTOL system and the above limitations, the boundary conditions can be given as follows:

$$U_d^2 + U_q^2 \leq U_{lim}^2 \tag{5}$$

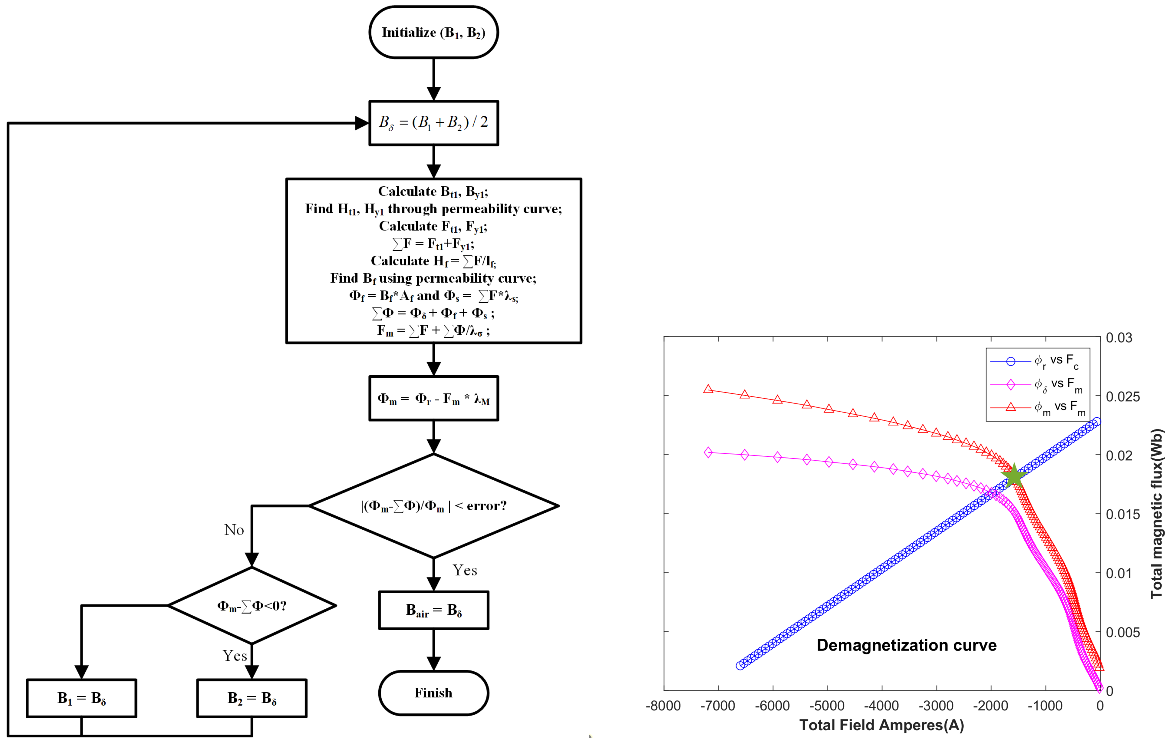

(a) (b)

Fig. 4 Magnet operation point (a) flowchart for solving magnet operation point and (b) Results of magnet operation point.

$$I_d^2 + I_q^2 \le I_{lim}^2 \tag{6}$$

Maximum voltage and current are considered to be constant during flux weakening operation. Based on Eq. 4 to Eq. 6, the steady-state voltage boundary equations can be expressed as follows:

$$\left(\frac{R_s I_d}{\omega} - L_q I_q\right)^2 + \left(L_d I_d + \frac{R_s I_q}{\omega} + \psi_m\right)^2 \le \frac{U_{lim}^2}{\omega} \tag{7}$$

The torque equation can be written as shown:

$$T_{em} = \frac{3}{2} p(\psi_m I_q + (L_d - L_q) I_d I_q) \tag{8}$$

As Eq. 7 shown, the voltage-limited boundary conditions are depicted as an ellipse whose area depends on the speed. The current limited equation is represented by a circle. Hence, any given operation point of PMSM does not exceed the lesser of the voltage limit ellipse and the current limit circle as shown in Fig. 5. In the flux weakening region, the operation point of the PMSM must be operated along the voltage limit ellipse, which indicates that the terminal voltage reaches its maximum value. Combining Eq. 7 and Eq. 8, the q-axis current in the flux-weakening condition can be expressed as a quadratic equation:

$$a_1 I_q^4 + a_2 I_q^3 + a_3 I_q^2 + a_4 I_q^1 + a_5 = 0 \tag{9}$$

$$\begin{cases} a_1 = 9p^2 (L_d - L_q)^2 (\omega^2 L_q^2 + R_s^2) \\ a_2 = 0 \\ a_3 = 9p^2 \psi_m^2 (R_s^2 + \omega^2 L_q^2) + 12 p \omega R_s T_{em} (L_d - L_q)^2 - 9p^2 (L_d - L_q)^2 U_{lim}^2 \\ a_4 = -12 p \psi_m T_{em} (\omega^2 L_d L_q + R_s^2) \\ a_5 = 4 R_s^2 T_{em}^2 + 4 L_d^2 \omega^2 T_{em}^2 \end{cases} \tag{10}$$

The above derivation shows that once the phase resistance and inductance at d- and q- axis have been solved using the MEC method, the q-axis current is determined by torque and speed:

$$I_q = f_1(T_{em}, n) \tag{11}$$

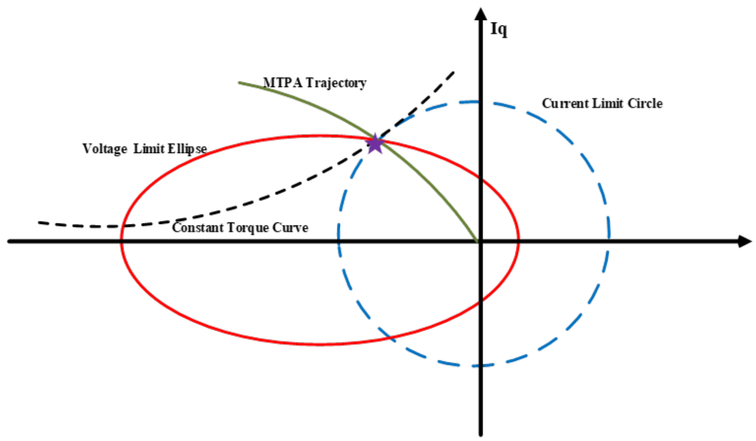

Fig. 5 Diagram of flux weakening and MTPA trajectory.

E. MTPA and Smooth Control

According to MTPA principle [14], for any reference torque, the d- and q-axis current should satisfy the following equations:

$$\begin{cases} \dfrac{\partial \frac{T_{em}}{I_{lim}}}{\partial I_d} = 0 \\ \dfrac{\partial \frac{T_{em}}{I_{lim}}}{\partial I_q} = 0 \end{cases} \tag{12}$$

Substituting Eq. 8 to Eq. 12, the per-unit q-axis current can be expressed as following:

$$I_q^{*4} + T_{em}^* I_q^* - T_{em}^{*\,2} = 0 \tag{13}$$

The q-axis current can be determined by the torque and speed:

$$I_q = f_2(T_{em}, n) \tag{14}$$

MTPA and flux weakening are two independent control strategies. To conserve computational resources and make the low-fidelity model compatible with the eVTOL optimizer, a smooth equation integrating MTPA and flux weakening was implemented. Based on the results of the large-scale sizing model and MEC analysis, these outputs are subsequently incorporated to determine the current based on operating voltage using a smoothed formulation of flux weakening and MTPA control. The flux weakening control operates at the maximum voltage limit, while MTPA governs the operation of motor below the voltage limit. In other words, the terminal voltage will determine the operation strategies of a PMSM during different voltage conditions. Based on the above discussion, the smooth equation can be expressed by Eq. 15; The result is shown in Fig. 6.

$$I_q = \frac{e^{k(U-U_{lim})} f_1(T_{em}, n) + e^{\frac{-1}{k(U-U_{lim})}} f_2(T_{em}, n)}{e^{k(U-U_{lim})} + e^{\frac{-1}{k(U-U_{lim})}}} \tag{15}$$

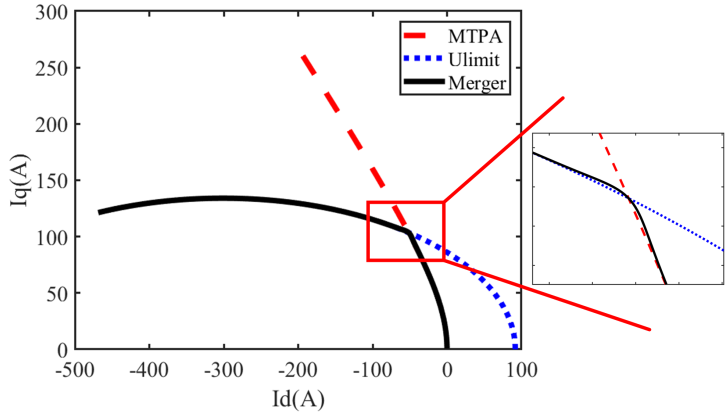

Fig. 6 Integrated curve between MTPA and flux-weakening.

IV. Validation

To validate the accuracy of the low-fidelity model, the PMSM model was simulated in MotorCAD software, an electromagnetic analysis software for the electric motor, compared with low-fidelity model results. An interior PMSM with 36 Slots and 12 poles has been studied. The motor geometry specification and electromagnetic properties of the motor are listed in Table 2. The validation criteria for the low-fidelity model are defined as follows. First, the magnetic and electric component, such as Back EMF, magnetic flux density, flux linkage, torque, and inductance, should be proven to equal the value calculated from the FEM software under different loading. In addition, the losses and efficiency map should be close to those computing using the FEM.

Table 2 Specification of PMSM

Items(Units)	Nomenclature	Value
Number of stator slots	Z	36
Number of pairs of pole	p	6
Rated Power (kW)	P_n	40
Rated Speed (RPM)	N_n	5000
Rated Torque (N.m)	T_n	73
Residual Flux density of magnets (T)	B_r	1.2
Internal Diameter of Stator (mm)	D_i	182
Outer Diameter of Stator (mm)	D_1	227.5
Effective length (mm)	l_{ef}	86

A. Comparison of Main Specification

Table 3 shows the comparison of the values of the key electromagnetic quantities and summarizes the error in percentage between low-fidelity model and FEM method. It can be seen that average deviation is around 4.5%. There are small deviation of 1.6% for torque at rated load, 1.5% for output power, which indicates a good match between FEM results and analytical model. The error of inductance at d-axis, q-axis and stator leakage reactance are -3.4%, 5.1%, and -6%, respectively. The back EMF is calculated on no-load condition, and the error is 7.2%. Flux linkage under load condition is also calculated, and the error is 8.5% compared with FEM results. Overall, the error is maintained within a moderate range in the context of all the benefits the proposed method offer.

Table 3 Comparison of main specification

Items(Units)	Analytical Results	FEM Results	Error (%)
Magnetic Flux Density (T)	0.6726	0.6552	2.6
Back EMF (V)	122.7	132.2	7.2
Flux Linkage (Wb)	0.0544	0.0595	8.5
Averagae Torque (N.m)	85.73	87.16	1.6
Output power (kW)	44.9	45.6	1.5
D axis inductance (mH)	0.0989	0.0956	3.4
Q axis inductance (mH)	0.286	0.272	5.1
Stator Leakage Reactance (Ω)	0.214	0.202	6

B. Comparison of Losses, Efficiency, and Computation Time

In the second step, losses and efficiency results are compared for the low-fidelity model and FEM results. Table 5 summarizes the respective loss values from between the two models under rated condition. The loss analysis equation are shown in Eq.16. The discrepancies are 2.4% and 1.8% for hysteresis loss and eddy loss in case of rated operation point, respectively. All of the errors are within 3%, which are acceptable in the low-fidelity model. Figure 7 shows the efficiency map calculated with the low-fidelity model. The rated operation point is in the area of maximum efficiency.

$$
\begin{aligned}
P_{cu} &= mI^2R_s \\
P_{hys} &= k_h\rho V f B^{n_h} \\
P_{eddy} &= K_e\rho V f^2 B^2 \\
P_m &= W_m n/n_N
\end{aligned}
\tag{16}
$$

Table 4 Comparison of losses and efficiency

Items(Units)	Analytical Results	FEM Results	Error (%)
Copper Loss (W)	978.38	978.4	0.002
Hysteresis Loss (W)	321.02	313.3	2.4
Eddy Loss (W)	288.478	294	1.8
Windage Loss (W)	102.52	100	2.5
Friction Loss (W)	102.52	100	2.5
Efficiency (%)	95.16	95.23	0.074

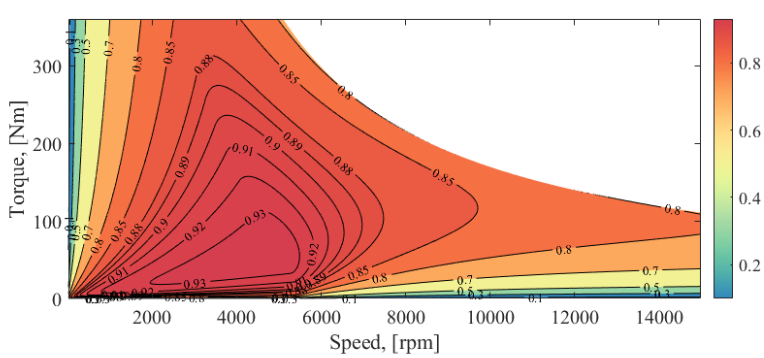

Fig. 7 Efficiency Map by Low fidelity model.

C. Computation Time

The computation time was compared for the low-fidelity model and FEM software using an AMD 5900HS processor and 40 GB installed memory operating Windows 11 system. Table 5 shows the computational time for the low-fidelity model and FEM method. As can be seen, the low-fidelity model has a very low computational cost compared with FEM method.

Table 5 CPU Time

	Low-fidelity model Time	FEM Time
Rated Load	3s	53s
Efficiency Map	33s	1258s

V. Conclusion

This paper presented a low-fidelity performance model for permanent-magnet synchronous motors that delivers comparable accuracy to FEA-based models but with much greater computational efficiency. The model uses a magnetic equivalent circuit model, empirical motor geometry model, and integrated control strategies. Compared with high-fidelity results in MotorCAD, the low-fidelity model achieved errors less than 10% for key parameters such as magnetic flux density, back EMF voltage, flux linkage, and average torque, for a 36-slot, 12-pole motor that was studied. Errors in the resulting losses and overall efficiency were less than 3%. This low-fidelity motor model is expected to be useful in computational methods for aircraft conceptual design, especially in system-level aircraft design optimization.

References

[1] Wheeler, P., Sirimanna, T. S., Bozhko, S., and Haran, K. S., "Electric/Hybrid-Electric Aircraft Propulsion Systems," *Proceedings of the IEEE*, Vol. 109, No. 6, 2021, pp. 1115–1127. https://doi.org/10.1109/JPROC.2021.3073291.

[2] Jayasinghe, S. G., Meegahapola, L., Fernando, N., Jin, Z., and Guerrero, J. M., "Review of Ship Microgrids: System Architectures, Storage Technologies and Power Quality Aspects," *Inventions*, Vol. 2, No. 1, 2017. https://doi.org/10.3390/inventions2010004, URL https://www.mdpi.com/2411-5134/2/1/4.

[3] Ganev, E., "Selecting the Best Electric Machines for Electrical Power-Generation Systems: High-performance solutions for aerospace More electric architectures." *IEEE Electrification Magazine*, Vol. 2, No. 4, 2014, pp. 13–22. https://doi.org/10.1109/MELE.2014.2364731.

[4] Ionel, D., Popescu, M., McGilp, M., Miller, T., and Dellinger, S., "Assessment of torque components in brushless permanent-magnet machines through numerical analysis of the electromagnetic field," *IEEE Transactions on Industry Applications*, Vol. 41, No. 5, 2005, pp. 1149–1158. https://doi.org/10.1109/TIA.2005.853377.

[5] Sizov, G. Y., Ionel, D. M., and Demerdash, N. A. O., "Modeling and Parametric Design of Permanent-Magnet AC Machines Using Computationally Efficient Finite-Element Analysis," *IEEE Transactions on Industrial Electronics*, Vol. 59, No. 6, 2012, pp. 2403–2413. https://doi.org/10.1109/TIE.2011.2163912.

[6] Liu, X., Lin, Q., and Fu, W., "Optimal Design of Permanent Magnet Arrangement in Synchronous Motors," *Energies*, Vol. 10, No. 11, 2017. https://doi.org/10.3390/en10111700, URL https://www.mdpi.com/1996-1073/10/11/1700.

[7] Hemeida, A., and Sergeant, P., "Analytical Modeling of Surface PMSM Using a Combined Solution of Maxwell–s Equations and Magnetic Equivalent Circuit," *IEEE Transactions on Magnetics*, Vol. 50, No. 12, 2014, pp. 1–13. https://doi.org/10.1109/TMAG.2014.2330801.

[8] Cao, Z., Huang, Y., Guo, B., Peng, F., Dong, J., and Hemeida, A., "A Novel Hybrid Analytical Model of Active Magnetic Bearing Considering Rotor Eccentricity and Local Saturation Effect," *IEEE Transactions on Industrial Electronics*, Vol. 69, No. 7, 2022, pp. 7151–7160. https://doi.org/10.1109/TIE.2021.3102396.

[9] Hwang, J. T., Lee, D. Y., Cutler, J. W., and Martins, J. R. R. A., "Large-Scale Multidisciplinary Optimization of a Small Satellite's Design and Operation," *Journal of Spacecraft and Rockets*, Vol. 51, No. 5, 2014, pp. 1648–1663. https://doi.org/10.2514/1.A32751, URL https://doi.org/10.2514/1.A32751.

[10] Hwang, J. T., and Ning, A., *Large-scale multidisciplinary optimization of an electric aircraft for on-demand mobility*, ???? https://doi.org/10.2514/6.2018-1384, URL https://arc.aiaa.org/doi/abs/10.2514/6.2018-1384.

[11] Mi, C., Filippa, M., Liu, W., and Ma, R., "Analytical method for predicting the air-gap flux of interior-type permanent-magnet machines," *IEEE Transactions on Magnetics*, Vol. 40, No. 1, 2004, pp. 50–58. https://doi.org/10.1109/TMAG.2003.821562.

[12] Htwe, N. H. H., "Design of 50 kw Permanent Magnet Synchronous Motor for HEV," 2019.

[13] Fouad, F. A., Nehl, T. W., and Demerdash, N. A., "Magnetic Field Modeling of Permanent Magnet Type Electronically Operated Synchronous Machines Using Finite Elements," *IEEE Transactions on Power Apparatus and Systems*, Vol. PAS-100, No. 9, 1981, pp. 4125–4135. https://doi.org/10.1109/TPAS.1981.316957.

[14] Zhao, S. F., Huang, X. Y., Fang, Y. T., and Li, J., "A control scheme for a High Speed Railway traction system based on high power PMSM," *2015 6th International Conference on Power Electronics Systems and Applications (PESA)*, 2015, pp. 1–8. https://doi.org/10.1109/PESA.2015.7398905.